PHYSICAL REVIEW E **113**, 014403 (2026)

Editors' Suggestion

Electric response of multiarm protein crystals

D. Ray,[1,2] F. Platten,[1,3] and K. Kang[1,*]
[1]Forschungszentrum Jülich, Institute of Biological Information Processing (IBI-4), Biomacromolecular Systems and Processes, Jülich, Germany
[2]Solid State Physics Division, Bhabha Atomic Research Centre, Trombay, India
[3]Faculty of Mathematics and Natural Sciences, Heinrich Heine University Düsseldorf, Düsseldorf, Germany

(Received 4 August 2025; accepted 1 December 2025; published 22 January 2026)

Electric fields can modify protein-protein interactions and thereby influence phase behavior. In lysozyme–sodium thiocyanate solutions, we recently observed shifts in both the crystallization boundary and the liquid-liquid phase separation line under a weak applied field, along with a range of distinct crystal morphologies. Here, we explore how forming protein crystals respond to variations in field frequency and amplitude, focusing on the morphologies of complex, multiarm structures. At constant protein and salt concentrations, the applied field governs both the number and the angular distribution of crystal arms. These features are analyzed through Fourier analysis of microscopy images, revealing cooperative angular ordering among the arms. Based on these observations, we classify three principal multiarm protein crystal (pX) morphologies: flowerlike pX (dominant at high field strengths), triconic pX (appearing nonmonotonically at lower fields), and conic pX (widely observed under low-field conditions). Near the crystallization boundary, field-driven metastable structures such as tubules, clusters, nematic domains, and fibers also occur in response to the field. These findings demonstrate that electric fields effectively steer protein crystallization pathways and provide insight into the mechanisms of various multiarm crystallization.

DOI: 10.1103/ql7f-wzpr

I. INTRODUCTION

Protein solutions exhibit a range of phase transitions, including crystallization, liquid-liquid phase separation (LLPS), cluster formation, fibrillation, and gelation [1–9]. Crystallization is of particular interest for structural biology, as large, well-ordered single protein crystals are required for X-ray diffraction and other structural methods. In some cases, crystallization is preceded by LLPS, especially in systems like lysozyme with added salts [e.g., NaCl, sodium thiocyanate (NaSCN)], where protein-rich and protein-poor phases form as an intermediate step [10,11].

As in other colloidal systems, interparticle interactions determine both the type of phase transitions and the kinetics of phase separation. Protein-protein interactions are sensitive to pH, salt type, and concentration, and the presence of additional precipitants such as polyethylene glycol or cosolvents [12–18]. Salt ions can alter these interactions through several mechanisms: by screening electrostatic repulsions, binding directly to protein surfaces (thereby reducing or reversing net charge), or forming ion bridges that promote attraction [19–21]. Ions can also modulate the protein hydration layer, potentially affecting conformation and stability [22,23].

These phenomena are collectively described by specific ion (Hofmeister) effects, which capture the role of ion identity beyond generic ionic strength [24]. Hofmeister effects significantly influence a wide range of physicochemical properties in protein solutions, including solubility [25–27], LLPS [28], adsorption [29], enzymatic activity [30], and electrophoretic mobility [19]. In LLPS, for instance, proteins often follow an inverse Hofmeister series at low salt concentration (salting out), which can reverse at high concentrations (salting in) [28]. Recent molecular theory explains this crossover as a competition between ion solvation energy and translational entropy, predicting the salting-in/salting-out transition [31]. These specific ion effects, in turn, have a direct impact on crystal nucleation and growth.

External electric fields offer an additional means to modulate protein-protein interactions and control phase behavior [32–38]. Electric fields can drive ion migration, alter local charge environments, and potentially influence protein alignment or orientation. We previously reported shifts in phase boundaries for lysozyme-NaSCN solution in the presence of a weak electric field [32]. The LLPS line shifts to higher NaSCN concentrations, while the crystallization boundary moves to lower concentrations. These trends are consistent with field-induced adsorption of SCN^- ions onto protein surfaces, which reduces their net charge and enhances interprotein attraction. This effect lowers the required bulk salt concentration for crystallization. In addition to these changes in phase boundaries, we also observed a pronounced

---

[*]Contact author: k.kang@fz-juelich.de

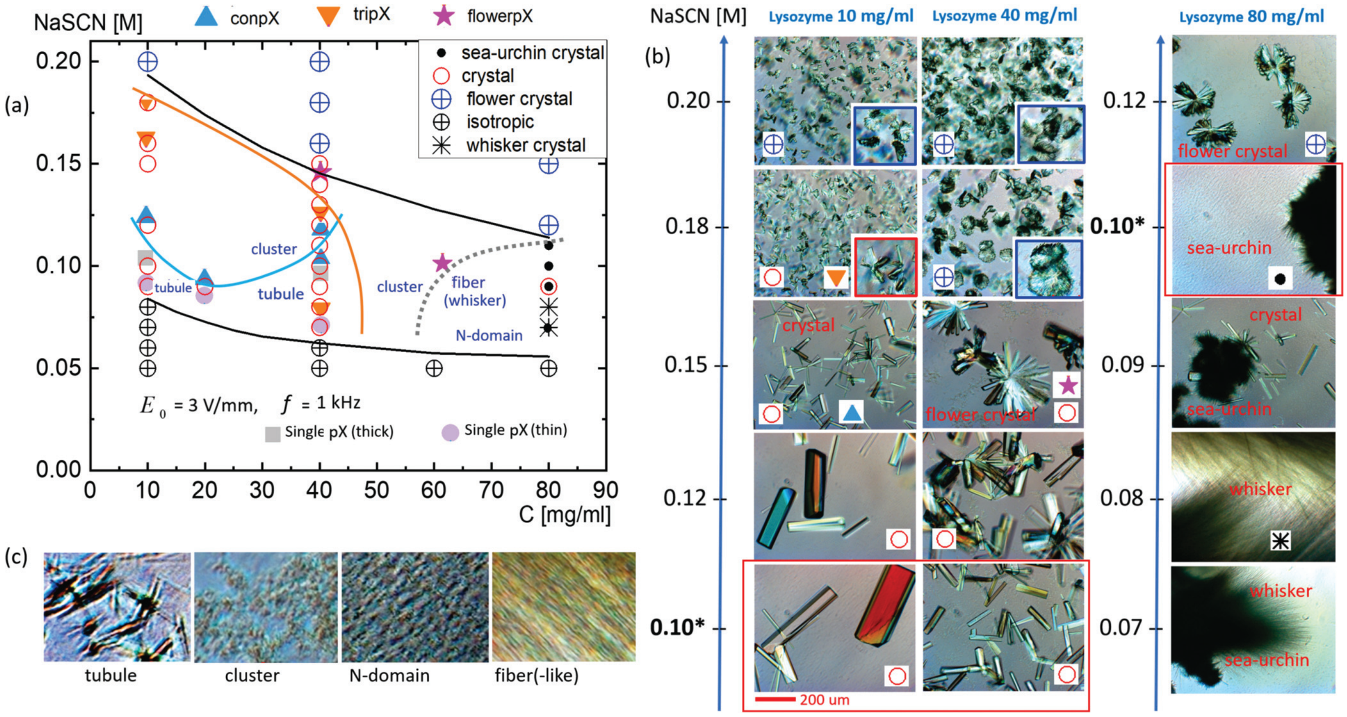

FIG. 1. Protein crystal morphologies under a given electric field: (a) Morphology-state diagram of lysozyme protein vs NaSCN concentration under an applied electric field of amplitude $E_0 = 3$ V/mm and frequency $f = 1$ kHz. The category labeled "crystals" in Ref. [33] is here refined into two subtypes: single-arm protein crystals (single pXs) and multi-arm protein crystals (multiarm pXs). The latter are further subdivided into three representative morphologies: conic pX (conpX), triconic pX (tripX), and flower pX (flowerpX), as discussed in the main text. Colored lines serve as guides to the eye, indicating regions where each multiarm morphology predominates, as discussed in the main text: blue (distinction between conpX and tripX), orange (distinction between tripX and flowerpX), and dotted black lines (distinction between flowerpX and fiber). The black lines mark the crystallization boundary (lower) and the liquid-liquid phase separation (LLPS) line (upper). (b) Representative polarized-light microscope images of crystal morphologies at selected NaSCN and protein concentrations (10 mg/ml, 40 mg/ml, and 80 mg/ml, as indicated). The thin red rectangles highlight the case of 0.1 M NaSCN detailed later. (c) Microscopy images of field-driven metastable morphologies observed near the crystallization boundary. These include tubules, clusters, nematic (N) domains, and fiber structures, which appear as protein concentration increases from left to right. The approximate regions where these morphologies occur are labeled in the morphology-state diagram (a).

influence of the electric field on the morphology of the resulting protein crystals [33]. In the absence of an applied field, multiple crystal forms commonly coexist, indicating substantial polymorphism. The application of an electric field suppresses this polymorphic diversity and selects for a single dominant crystal morphology. Although external electric fields can, in principle, also perturb the protonation equilibrium of surface residues, the field strengths employed here are too weak to induce significant amount of protons in the pKa shift. Therefore, direct field-induced protonation effects are expected to be minor compared to polarization and ion adsorption contributions.

In this study, we systematically investigate how variations in electric field frequency and amplitude affect the morphology of protein crystals. We focus on the emergence of complex architectures under field conditions, with particular attention to the late-stage multiarm morphologies. They differ in number of arms and their angular distribution. These structures, defined by multiple crystal arms radiating from a common center, suggest that nucleation may involve several prealigned subnuclei, each giving rise to a distinct arm. Fourier analysis then reveals cooperative angular ordering among the arms. Based on these observations, we identify representative types of multi-arm protein crystal (pX), namely, flowerlike, triconic, and conic.

We propose that field-induced polarization governs both the angular arrangement of arms and the selection of crystal growth pathways. Figure 1 provides the morphology-state diagram for lysozyme-NaSCN solutions under an applied electric field of amplitude $E_0 = 3$ V/mm and frequency $f = 1$ kHz. This serves as the reference condition for our analysis of field-induced effects and is discussed in detail in Sec. III. We provide a comprehensive mapping of the protein crystal morphologies, extensively collected by the electric response of a multiarm protein crystal as a function of field frequency and amplitude.

II. EXPERIMENTAL METHODS

The experimental procedures largely follow those of our previous studies [32,33]. For completeness, a brief summary of sample preparation and electric field setup is provided below. Lysozyme solutions were prepared in 50 mM sodium acetate buffer (pH 4.5) with NaSCN as the crystallizing agent.

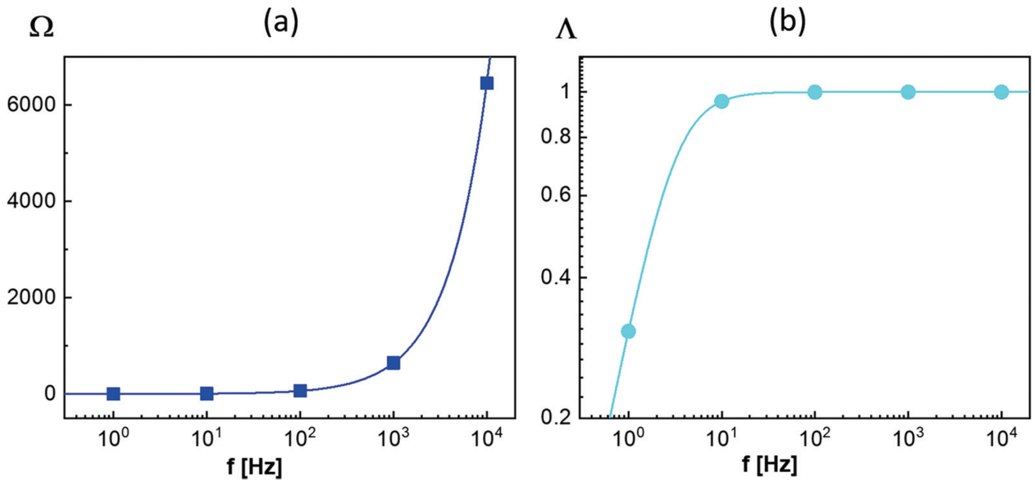

FIG. 2. Characteristic parameters of the electric field experienced by the particles within the bulk solution as a function of field frequency f [40,41]: (a) The dimensionless frequency, $\Omega = \omega L/(D\kappa)$, where $\omega = 2\pi f$ is the angular frequency, $\kappa^{-1} \approx 0.96$ nm is the Debye screening length, $L \approx 160$ μm is the electrode gap, and $D \approx 1.5 \times 10^{-9}$ m^2/s is the diffusion constant at 0.10 M NaSCN salt. (b) The attenuation factor, given by $\Lambda = \Omega/\sqrt{4 + \Omega^2}$, which describes the ratio of the field amplitude within the bulk to the applied field amplitude. Note that due to electrode polarization, the electric field amplitude within the bulk of the solution is reduced compared to the externally applied field, as electric double layers at the electrodes partially screen the applied electric potential.

Samples were prepared by mixing defined volumes of protein and salt stock solutions with buffer, as detailed in our previous work [32,39]. All experiments were conducted at (24 ± 1) °C.

AC electric fields were applied using a Siglent SDG830 function generator and a custom-built sample cell with transparent indium tin oxide–coated glass electrodes, as described in [32,33]. The field conditions are varied by frequency f (10 Hz–10 kHz) and amplitude E_0 (0–30 V/mm) to examine their influence on protein crystal morphology formation. The sample cell thickness was 0.16 mm. The microscopic crystal morphology was monitored under an inverted polarized-light microscope (Zeiss Axiovert 40CFL) equipped with an AxioCam Color CCD camera.

In the presence of a weak AC electrical field, two parameters characterize the electric field experienced by particles in bulk solution, which are illustrated for the dimensionless frequency in Fig. 2(a) and the attenuation factor in Fig. 2(b). The dimensionless frequency, $\Omega = \omega L/(D\kappa)$, where $\omega = 2\pi f$ is the angular frequency, κ^{-1} is the Debye screening length, and D is the diffusion constant at 0.10 M NaSCN salt. The attenuation factor, given by $\Lambda = \Omega/\sqrt{4 + \Omega^2}$, compares the amplitude of the field experienced by the particles to the applied field amplitude E_0. The origin of the attenuation factor, used to estimate the field amplitude experienced by the particles, as well as the resulting electric polarization is supported by both theory and experiment [40,41]. Notably, in this system, a distinct transition occurs at applied frequencies around 1 Hz ($\Lambda \ll 1$) and 10 Hz ($\Lambda \approx 1$).

III. PROTEIN CRYSTAL MORPHOLOGIES UNDER ELECTRIC FIELDS: CLASSIFICATION OF MULTIARM STRUCTURES

In our previous study [33], where we compared systems with and without this specific field, we identified four main morphological categories: crystals, flower crystals, whisker crystals, and sea urchin crystals, along with an isotropic solution phase [see top-right legend in Fig. 1(a)]. The category previously referred to as "crystals" is now more finely subdivided, and its members are collectively designated as *pXs*. This class is divided into two main types: single pXs and multiarm pXs. Single pXs are compact, birefringent crystals exhibiting minimal anisotropy, appearing as either small or large particles. In contrast, multiarm pXs exhibit pronounced anisotropic branching and are further classified into three characteristic morphologies based on arm symmetry and arrangement: conic pX (*conpX*), featuring fanlike arm spreading; triconic pX (*tripX*), typically displaying three arms separated by approximately 120°; and flowerlike pX (*flowerpX*), characterized by radially symmetric, lobed structures with increased arm number and morphological complexity.

The spatial distribution of these types in the phase diagram is shown in Fig. 1(a). ConpX morphologies prevail above the blue line, tripX morphologies dominate below the orange line, and flowerpX structures typically occupy the region above the orange line or at high protein concentrations. All three appear in the zone between the crystallization boundary and the LLPS line, where electric field effects most strongly modulate symmetry, branching, and arm number.

Beyond these three multiarm pX morphologies, additional variants emerge near the crystallization boundary and LLPS line. Close to the crystallization line, we occasionally observe asymmetric flowerlike morphologies (*AfpX*) and superpositions of tripX-like motifs. These are likely the result of field-induced symmetry breaking or anisotropic nucleation events. At higher protein concentrations, just above the LLPS line, compact, radially symmetric flower crystals appear (e.g., at 80 mg/ml lysozyme and 0.12 M NaSCN). These are distinct from the flowerpX class and form in the unstable regime beyond the crystallization region. In contrast, flowerpX morphologies are observed at intermediate protein concentrations (e.g., 40 mg/ml) and slightly higher salt concentrations (0.12–0.15 M NaSCN). At very high protein concentrations, anisotropic growth forms such as sea urchins and whiskers emerge. These suggest different underlying growth mechanisms, possibly dominated by directional interactions and density-driven aggregation.

Figure 1(b) shows polarized-light microscopy images for representative concentrations. For a low protein concentration of 10 mg/ml and NaSCN concentrations below 0.12 M, large single pXs are the dominant crystal morphology. These crystals exhibit strong birefringence, with characteristic color transitions (blue, green, red) indicating increasing optical path length due to crystal thickness. In contrast, multiarm pX types become prevalent at intermediate protein concentrations (40–80 mg/ml), with specific morphologies correlating with regions defined in Fig. 1(a). FlowerpX crystals, for instance, are frequently observed near 40 mg/ml and 0.12–0.15 M NaSCN.

As shown in Fig. 1(c), metastable morphologies such as tubules, clusters, nematic (N) domains, and fibers emerge near the crystallization boundary. These structures indicate that the applied electric field perturbs local thermodynamic conditions and promotes transient network formation. In lysozyme-NaSCN solutions, specific ion effects, most notably the chaotropicity of SCN^-, are known to modulate protein-protein attractions and enhance structural heterogeneity. The electric field amplifies these effects by driving local ion redistribution, altering adsorption layers, and imposing orientational constraints on early aggregates. Such metastable states suggest that weak fields influence not only the orientational bias during nucleation but also the subsequent mesoscale growth pathways. This field-ion coupling between the ionic environment and orientational order plays a central role in shaping the final crystal morphologies.

The observed variety of multiarm pX morphologies likely reflects underlying polarization mechanisms that vary with protein concentration: (i) At low concentrations, dielectric contrast (i.e., the permittivity difference between protein and solvent), together with surface charging, plays the dominant role. This leads to large variances in crystal size and shape anisotropy (e.g., the large single red pX at 10 mg/ml lysozyme and 0.1 M NaSCN), due to electric polarization effects. (ii) At intermediate concentrations, polar and quadrupolar modes compete to maintain finite crystal sizes. (iii) At high concentrations, quadrupolar polarization becomes more significant, resulting in increased local crowding and multipolar interactions, with field-induced rigid whiskers and sea-urchin-like structures that may also form without a field. These concepts will be further explored in the following sections, relating angular arm distributions to field-induced polarization modes and their symmetry implications.

IV. FIELD AMPLITUDE AND FREQUENCY DEPENDENCE

Figures 3(a) and 3(b) present representative polarized-light microscopy images at a fixed protein concentration of 40 mg/ml and a NaSCN concentration of 0.10 M, illustrating the diversity of protein crystal morphologies that emerge under varying electric field conditions. Two types of field variation are shown: (i) frequency variation from 10 Hz to 10 kHz at a constant field amplitude of $E_0 = 3$ V/mm in Fig. 3(a), and (ii) field amplitude variation from 0 to 30 , V/mm at three fixed frequencies (10 Hz, 100 Hz, and 1 kHz) in Fig. 3(b).

Under all tested field conditions, we observe exclusively crystal (pX) morphologies, with significant variation in arm number and orientation. As shown in Fig. 3(a), lower frequencies predominantly produce single pXs, whereas higher frequencies promote multiarm structures. Similarly, Fig. 3(b) shows that low field amplitudes favor single pXs or crystals with fewer arms, while higher amplitudes lead to more complex multiarmed morphologies. Although not strictly monotonic, the general trend indicates that increasing frequency and amplitude correlate with an increasing number of crystal arms.

The observed variations in crystal morphology are qualitatively interpreted in terms of field-modulated polarization effects, drawing on theoretical insights from nonlinear electrostatics in electrolyte systems [42]. We hypothesize that morphological features, such as the number, symmetry, and orientation of crystal arms, reflect distinct polarization responses induced by the electric field. These features are schematically abstracted in Fig. 3(c), providing a conceptual link between field-induced polarization mechanisms and the resulting morphological symmetry breaking, i.e., the emergence of preferred crystal shapes and growth directions under the influence of an electric field, as well as the shift of chemical equilibrium. Since protein crystal growth is known to proceed via the addition of monomeric growth units [43], the concept of a field-dependent association constant may be more relevant to the growth process itself, not only to nucleation.

Different crystal morphologies thus reflect electric responses of polarization: More symmetric, radially aligned structures such as flowerpX may correspond to relatively uniform polar responses, while asymmetrically distorted forms such as AfpX could be associated with directional, dipolelike alignment. Some crystals also exhibit features consistent with nonpolar, possibly quadrupolarlike organization.

In several cases, multiple polarization features appear to coexist, forming what may be described as a mixed state that combines asymmetric, dipolarlike and symmetric, nonpolar regions. This is especially apparent in large triconic-pX structures. Schematic representations of these field-influenced morphologies, along with their corresponding angular distributions, are shown in Fig. 3(d). The characteristic angle θ between adjacent arms provides a geometric basis for distinguishing between conpX, tripX, and flowerpX morphologies. While speculative, this interpretation offers a qualitative link between electric field effects and the symmetry-breaking processes that shape protein crystal growth.

To systematically investigate how electric field parameters influence protein crystallization, we varied both the field amplitude and the frequency, extending beyond the previously studied conditions ($E_0 = 3$ V/mm, $f = 1$ kHz) reported in [32,33]. All experiments were performed at a fixed solution composition of 40 mg/ml lysozyme and 0.10 M NaSCN, under which multiarm pX morphologies have been reported earlier [32]. The microscopy data obtained across the full range of field parameters are summarized in the electric state diagram shown in Fig. 4(a), where each observed crystal morphology is mapped as a function of electric field amplitude and frequency. Representative microscope images corresponding to each morphology are presented in Fig. 4(b).

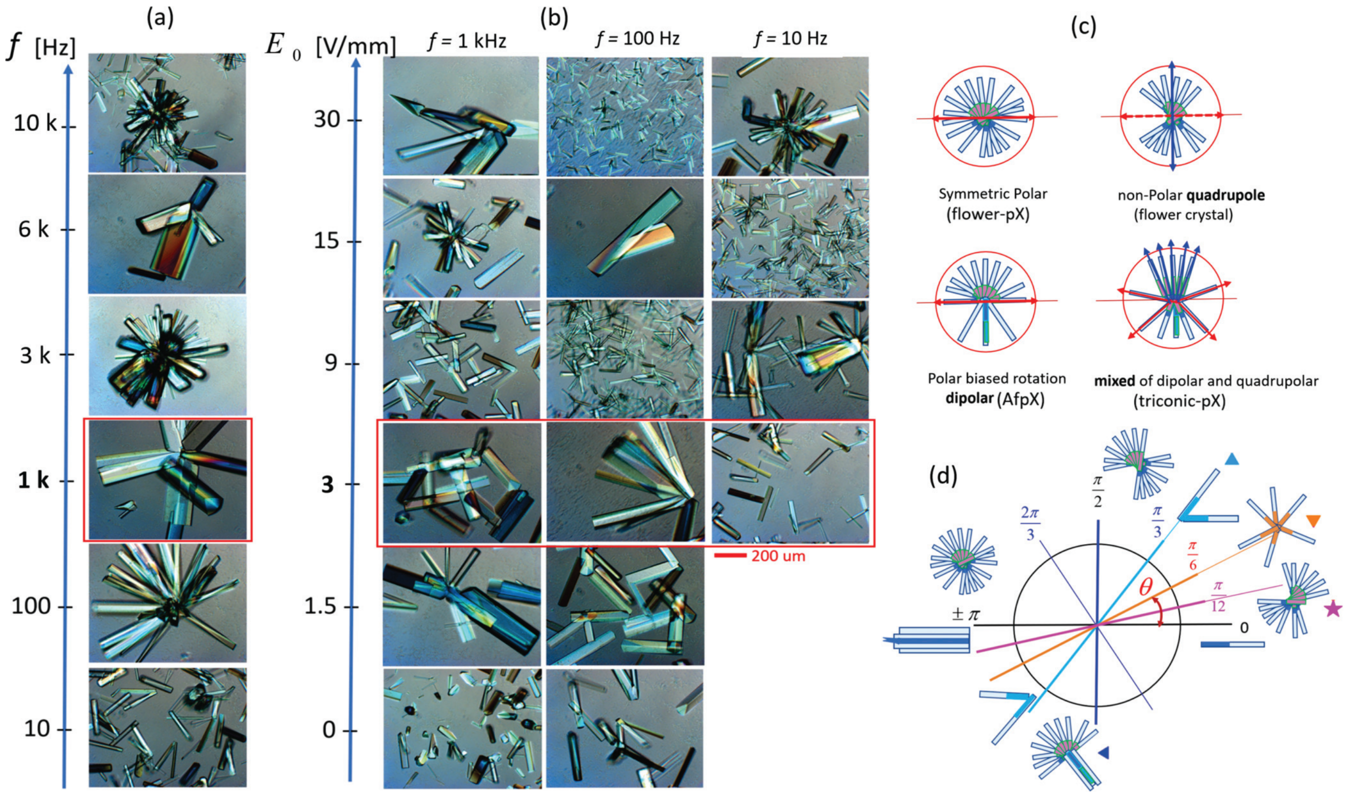

FIG. 3. Morphologies of protein crystals with multiple arms formed under various electric field amplitudes and frequencies: (a) Polarized light microscopy images of crystals formed at different frequencies (as indicated) with fixed field amplitude $E_0 = 3$ V/mm. (b) Morphologies obtained at different field amplitudes (as indicated) for three selected frequencies: 10 Hz, 100 Hz, and 1 kHz. In both (a) and (b), the protein concentration is 40 mg/ml and the NaSCN concentration is 0.10 M. Red rectangles highlight the field condition investigated in Fig. 1. (c) Conceptual sketches illustrating possible polarization-driven mechanisms underlying morphological diversity. (d) Schematic representation of angular distributions associated with different crystal symmetries, which serve to qualitatively relate the observed arm orientations to field-induced polarization modes, ranging from uniform alignment to asymmetric or quadrupolarlike organization. The characteristic angle θ is illustrated for three representative pXs: flowerpX ($\theta = \pi/12, 11\pi/12$), tripX ($\theta = \pi/6$), and conpX ($\theta = \pi/3$).

Morphologies are distinguished based on the number and angular distribution of crystal arms, as illustrated in the insets of Fig. 4(a). The red horizontal and vertical lines in Fig. 4(a) mark the field conditions previously used in Refs. [32,33].

The key features emerging from this state diagram and the supporting microscopy images are summarized as follows:

First, smaller flowerpX structures are predominantly observed at frequencies above $f = 1$ kHz, in the region above the solid purple line in Fig. 4(a). At lower frequencies, asymmetric flowerpX (AfpX) and single-pX morphologies are more commonly found.

Second, similarly, the transition to tripX morphologies occurs above the solid orange line, with a sharp increase in their appearance near $f \approx 1$ kHz, suggesting a frequency-sensitive threshold.

Third, several additional morphologies are identified and marked in the diagram. AfpX denotes asymmetric flowerlike crystals, while *pXA* refers to elongated groupings of aligned single pXs. The label *pXn* is assigned to densely packed clusters of unaligned single pXs, appearing either as randomly distributed aggregates or as compact groupings. *pXj* designates jointed structures composed of stacked crystals with nonuniform arm thickness. Together, these categories encompass the intermediate and clustered states observed beyond the principal single- and multiarm pX types.

Fourth, although a wide range of angular distributions and arm symmetries is observed across the parameter space, the dependence on frequency appears more pronounced than that on field amplitude. Increasing the field amplitude tends to produce more irregular and less predictable shapes, as seen in Fig. 3(b). Nevertheless, flowerpX, tripX, and conpX morphologies can consistently be identified across a wide range of field conditions, as delineated by the colored boundary lines in Fig. 4(a).

V. FOURIER ANALYSIS OF FIELD FREQUENCY DEPENDENCE

To quantify the averaged angular arrangement of crystal arms under varying electric field conditions, we analyze polarized light microscopy images via two-dimensional Fourier transforms (FTs). For a single elongated object, such as a linear crystal arm, the FT produces a characteristic sinclike intensity distribution, featuring a central maximum and side lobes aligned perpendicular to the long axis of the object. This basic property means that the FT intensity pattern directly encodes the orientation of the object in reciprocal space.

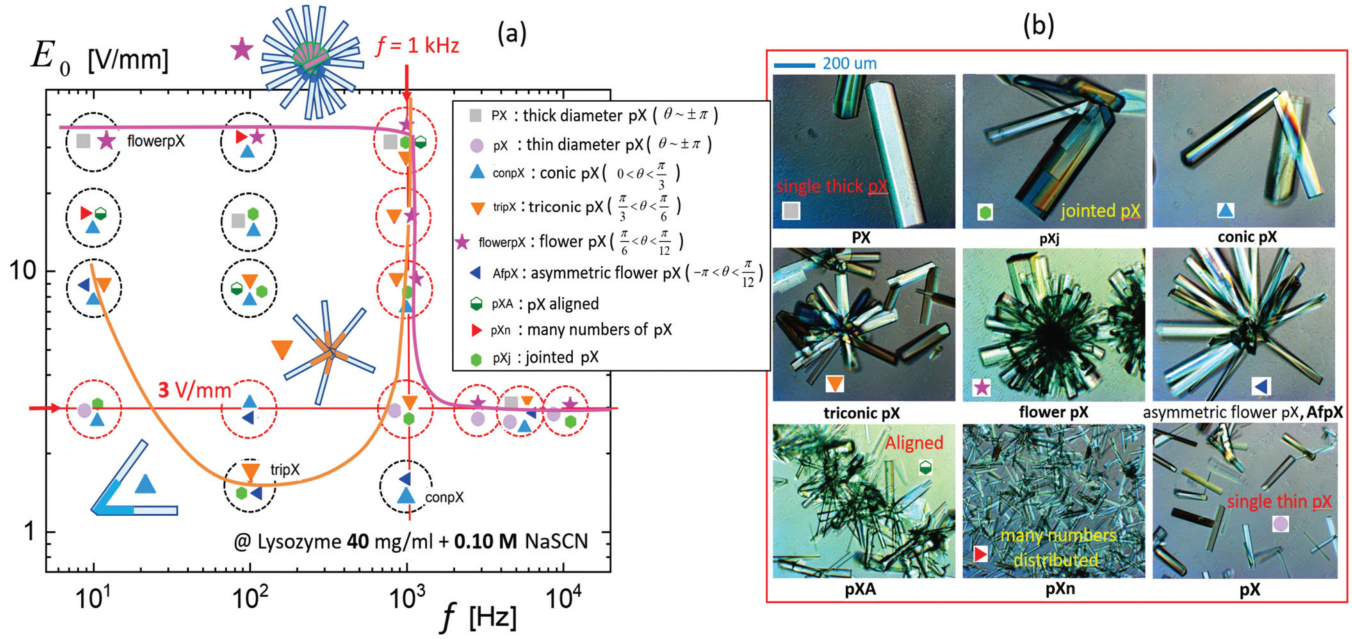

FIG. 4. The electric state diagram of multiarm protein crystal morphologies: (a) The electric state diagram in the field amplitude E_0 and frequency f plane, at a fixed protein concentration of 40 mg/ml and salt concentration of 0.10 M, such that multiarm protein crystal morphologies are grouped into three principal categories: conic pXs (conpX), triconic pXs (tripX), and flowerlike pXs (flowerpX), along with other subtypes. The red lines and arrows mark the reference field conditions studied in Fig. 1. The solid purple line indicates the region above which flowerpXs appear at high field strengths. The orange line separates the region above which tripXs are observed, while conpXs and occasional asymmetric flowerlike morphologies (AfpX) appear below it. (b) Representative microscopy images of the various multiarm protein crystal morphologies, labeled with the corresponding symbols used in panel (a) and described in the main text.

Extending this concept to multiarm protein crystals, each arm similarly contributes a radial streak in Fourier space, perpendicular to its orientation.

The superposition of these individual streaks yields a complex pattern of multiple radial lobes, where the number and angular positions of these streaks reflect the symmetry and orientation of the crystal arms. The angular sharpness of these lobes correlates with arm length: longer arms produce narrower, more defined peaks. Even in heterogeneous ensembles with some variability, statistically dominant arm orientations manifest as persistent intensity peaks in the FT, making this approach a robust method to extract and quantify orientational order in the crystal morphology.

Figure 5 shows Fourier-transformed microscopy images of protein crystals recorded without an electric field and under a fixed field amplitude of $E_0 = 3$ V/mm at increasing field frequencies of 10 Hz, 100 Hz, and 1 kHz [44]. In the absence of a field and at the lowest frequency (10 Hz), the Fourier pattern exhibits a broad, nearly symmetric distribution of angular streaks, consistent with an isotropic or only weakly ordered crystal ensemble. At intermediate frequency (100 Hz), the pattern develops a marked asymmetry, showing two dominant streaks of unequal intensity mirrored about the reference direction. At the highest frequency (1 kHz), the Fourier transform displays a narrow, intense directional peak accompanied by weaker features, indicating a strongly aligned state with preferential arm growth along a single axis and a higher degree of orientational order.

These qualitative differences are quantified in Fig. 6, where the angular intensity distribution $P_K(\theta_K)$ is extracted from the Fourier patterns. Here, θ_K denotes the angular separation of arms relative to a fixed reference, shown in the transformed images. The full angular range $-\pi < \theta_K < \pi$ is retained, as allowed by the use of polarized light, enabling the detection of directional (vectorial) asymmetries that would otherwise be lost in π-periodic methods.

The analysis identifies a hierarchy of intensity peaks, ranked by their magnitude: the primary peak (indicated as “1st”) corresponds to the dominant arm orientation, while the secondary peak (indicated as “2nd”) presents an orthogonal direction. Of particular interest is the tertiary peak (indicated as “3rd”), which, although weaker, appears at distinct angular positions suggestive of local deviations from global symmetry—interpreted as signatures of locally twisted orientations or subtle arm bending within the crystal structure. This nuanced peak evolution implies a continuous progression from symmetric distributions at low frequencies to highly asymmetric and locally distorted patterns at high frequencies, with an intermediate antisymmetric regime where two dominant orientations of unequal intensity coexist. Such complexity in the angular spectrum indicates a frequency-dependent reorganization of crystal arm growth cooperatively influenced by the external field.

Importantly, the Fourier-based orientation analysis aligns closely with the field-induced morphological changes discussed earlier. The emergence of antisymmetric angular distributions at intermediate frequencies correlates with the prevalence of tripX-type morphologies, with arms typically separated by about 120°. At high frequencies, where flowerpX morphologies dominate, the corresponding Fourier signatures

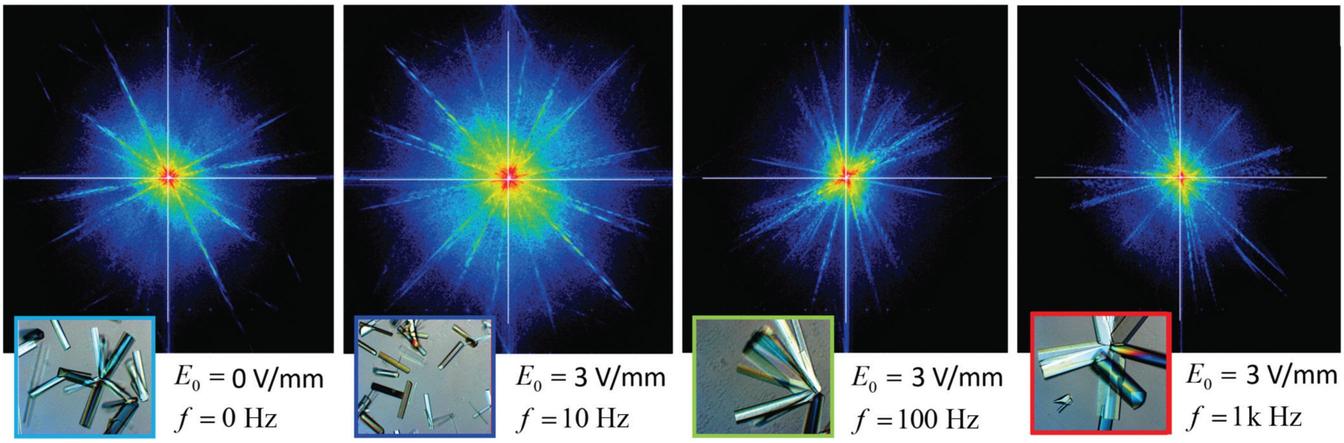

FIG. 5. Fourier-transformed microscopy images of multiarm protein crystals: For the protein concentration of 40 mg/ml, and a NaSCN concentration 0.10 M), without and with an applied electric field of fixed amplitude $E_0 = 3$ V/mm at different field frequencies (10 Hz, 100 Hz, and 1 kHz). The corresponding real-space microscopy images are shown as insets, all taken from the same field of view as in Fig. 3. Without field, single pX and tripX coexist. At 10 Hz, single-arm pX dominate with uniform orientation. At 100 Hz, conpX prevail, shown by asymmetric Fourier peaks. At 1 kHz, a narrow, intense peak indicates strong alignment consistent with tripX and flowerpX formation.

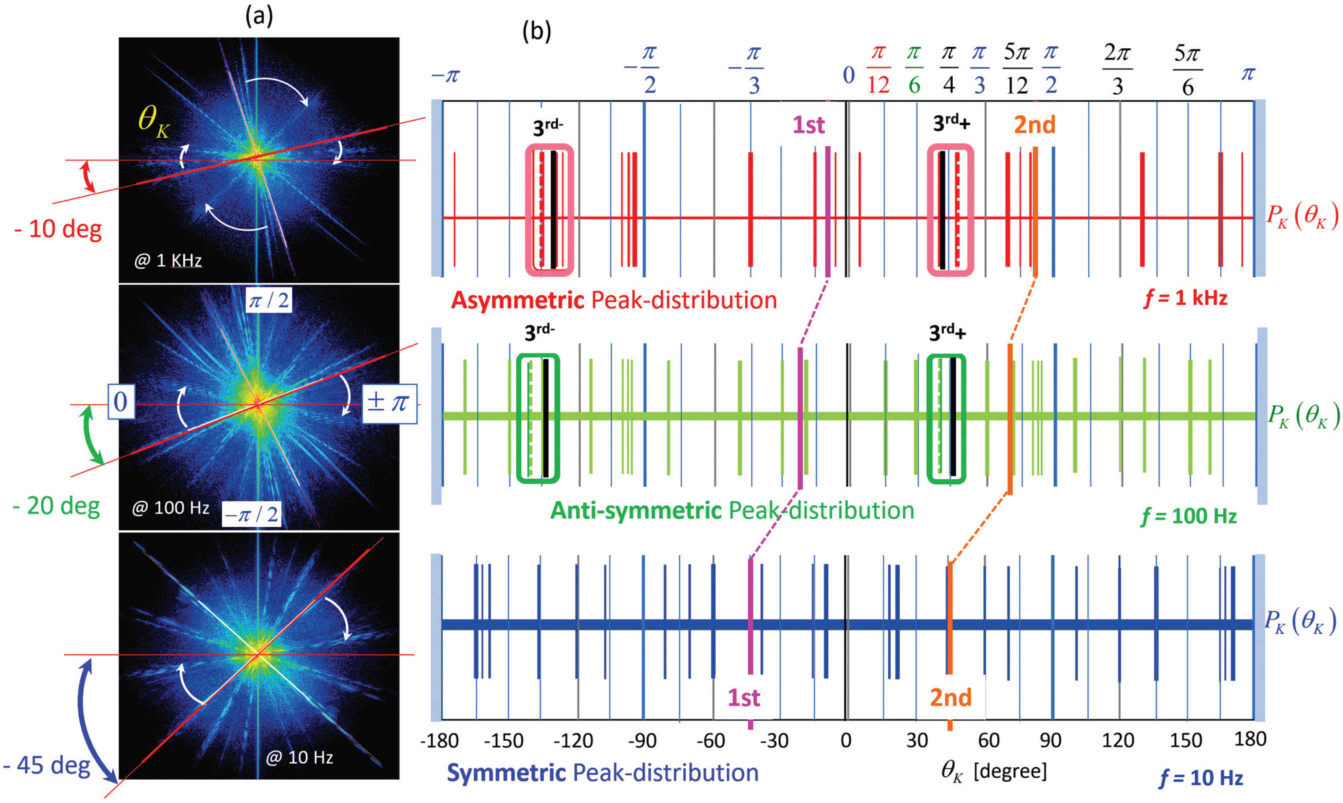

FIG. 6. Fourier analysis of crystal arm orientations at different field frequencies: (a) Fourier-transformed microscope images of multiarm protein crystals, showing the spatial distribution of arm orientations at increasing field frequencies (from bottom to top). All images correspond to a fixed field amplitude of 3 V/mm, for lysozyme at 40 mg/mL in 0.10 M NaSCN. (b) Corresponding angular distributions of the Fourier intensities, presented linearly along the angular axis. Only the angular positions at which intensity peaks occur are indicated. The peak angle θ_K indicates the dominant orientation between arms, measured with respect to a reference arm [red horizontal lines in (a)], and is shown within the range $0 < \theta_K < \pi$ and $-\pi < \theta_K < 0$. The distributions reveal frequency-dependent shifts in the primary and secondary peaks (labeled as "1st" and "2nd" in the figure), as well as symmetry changes in third- and higher-order orientations (e.g., marked by the angle between dashed and solid black lines).

display narrow, intense peaks, indicative of long arms aligned along a single or a few preferred directions. Thus, the symmetry of angular orientation distributions encodes key features of the underlying morphologies. Interestingly, the molecular configuration of heavy atom groups in protein crystals can also be determined by Fourier map analysis [45].

Although the Fourier analysis is inherently limited to two-dimensional projections, the observed asymmetries provide valuable insight into the three-dimensional ordering tendencies of the system. The increasingly directional alignment at higher frequencies suggests that the applied electric field does not merely influence local growth dynamics, but also promotes collective orientation across the entire ensemble. This observation supports the broader physical picture that external fields modulate polarization responses at the crystal-solution interface, thereby affecting both the number and spatial orientation of arms during crystallization. The connection between field-induced polarization effects and the emergent orientational order has also been discussed in the context of Figs. 3(c) and 3(d).

VI. CONCLUSION

We have demonstrated that weak AC electric fields systematically influence protein crystal morphology, particularly promoting multiarm structures in lysozyme-NaSCN solutions at fixed composition. By varying the field amplitude and frequency, we identified three characteristic (shape) morphologies—flowerpX, tripX, and conpX—each favored under distinct field conditions. These morphologies differ in arm number, angular orientation, and internal symmetry, underscoring the field capacity to modulate crystallization pathways between the LLPS and crystallization boundaries. Our observations indicate that the applied field affects both nucleation and growth stages, by altering local polarization fields and enhancing anisotropy in intermolecular interactions. Fourier analysis further reveals frequency-dependent cooperative alignment of arm orientations, indicative of collective field-induced ordering processes.

The formation of multiarm crystals shows a robust dependence on field amplitude and frequency. FlowerpX structures dominate at high field strengths, tripX forms appear nonmonotonically at intermediate values, and conpX configurations prevail across a broad low-field regime. This sequence is captured in an electric state diagram mapping crystal types as a function of field parameters. These transitions reflect a field-driven reorganization of local anisotropic interactions, involving both polar and quadrupolar ordering. Symmetric polar alignments in flowerpX evolve into asymmetric dipolar states (AfpX) and ultimately into nonpolar, twisted triconic arrangements. These morphological changes are echoed in the Fourier angular spectra, where secondary and tertiary peaks, ranked by Fourier intensity, trace the emergence of preferred orientations beyond simple dipolar order. Notably, the tertiary peak often corresponds to locally twisted or frustrated configurations arising under intermediate-frequency conditions.

We also observe that varying field parameters modulates metastable network structures, such as tubules, clusters, and nematic domains, which become increasingly prominent near the crystallization boundary. Altogether, the Fourier analysis reveals a frequency-driven shift from symmetric to asymmetric orientational distributions, consistent with enhanced anisotropy and collective alignment under field control.

Finally, we conclude these findings establish that weak electric fields provide a powerful means to tune not only the symmetry and morphology of protein crystals but also the dominant formation pathways. Such field-induced control opens avenues for tailoring crystallization in biological and soft matter systems. Future studies combining *in situ* microscopy with scattering or spectroscopic probes will be essential to unravel the microscopic mechanisms behind these field-mediated effects.

ACKNOWLEDGMENTS

We thank Jan K. G. Dhont for his valuable comments and helpful discussions on electric field effects on proteins. We acknowledge the German Research Foundation (DFG) for funding our project on protein phase behavior in electric fields (Project No. 495795796).

DATA AVAILABILITY

The data are available from authors upon reasonable request.

APPENDIX: DISPLACEMENT OF DIELECTRIC SUSCEPTIBILITY IN POLARIZATION AND ABSORPTION

In the experiment, the interaction between the lysozyme-NaSCN solution and the crystal surface is influenced by the frequency-dependent dielectric properties of both the solution and the protein crystal under the applied electric field. Most materials possess a complex, frequency-dependent dielectric constant $\epsilon(\omega)$, which reflects both static (zero frequency) and dynamic polarizability due to field-induced polarization [46].

Under a weak alternating electric field, the displacement field D can be expressed as $D = \epsilon_s E = E + 4\pi P$, where ϵ_s is the static dielectric constant, and $P = \chi E$ is the polarization, with χ denoting the electric susceptibility. For a time-dependent field $E(t) = E_0 \cos(\omega t)$, the field-induced polarization exhibits a phase lag relative to the driving field. The displacement field can be expressed using a memory kernel of $\varphi(t)$ as $D(t) = E(t) + \int_0^t E(t')\varphi(t-t')\mathrm{d}t'$, where $t - t'$ is the retardation time and t' is a dummy time variable.

In the frequency domain, the response of complex dielectric function is related by the Kramers-Kronig relations, as $\epsilon(\omega) = \epsilon'(\omega) + i\epsilon''(\omega)$, where the real and imaginary parts are given by $\epsilon'(\omega) \sim \int_0^\infty \varphi(t)\cos(\omega t)\mathrm{d}t$ and $\epsilon''(\omega) \sim \int_0^\infty \varphi(t)\sin(\omega t)\mathrm{d}t$.

Also, in the low-frequency limit, the dielectric constant is related to the refractive index n by $\epsilon \approx n^2$. The absorption of an electromagnetic wave in the medium is characterized by an exponential attenuation of the field intensity: $I = I_0 \exp(-\alpha x)$, where α is the absorption coefficient, approximately given by $\alpha(\omega) = 2\omega\tilde{\kappa}c \sim \omega\epsilon''(\omega)$, with $\tilde{\kappa}$ denoting the extinction coefficient (to be distinguished from κ, the inverse Debye length) and c the speed of light. The imaginary part of the dielectric function $\epsilon''(\omega)$ thus directly determines the absorption.

In this study, the frequency- and amplitude-dependent response of the protein solution to the applied field is reflected in the observed crystal morphologies. For instance, the observed color variations in the microscopy images arise from differences in optical path length, caused by variations in crystal thickness and birefringence. These color changes thus provide indirect information about the spatial distribution of structural ordering within the crystals.

[1] A. Stradner and P. Schurtenberger, Soft Matter **16**, 307 (2020).

[2] R. Mezzenga and P. Fischer, Rep. Prog. Phys. **76**, 046601 (2013).

[3] J. J. McManus, P. Charbonneau, E. Zaccarelli, and N. Asherie, Curr. Opin. Colloid Interface Sci. **22**, 73 (2016).

[4] C. R. Berland, G. M. Thurston, M. Kondo, M. L. Broide, J. Pande, O. Ogun, and G. B. Benedek, Proc. Natl. Acad. Sci. USA **89**, 1214 (1992).

[5] A. C. Dumetz, *et al.*, Biophys. J. **94**, 570 (2008).

[6] A. Stradner, G. M. Thurston, and P. Schurtenberger, J. Phys.: Condens. Matter **17**, S2805 (2005).

[7] O. Galkin and P. G. Vekilov, Proc. Natl. Acad. Sci. USA **97**, 6277 (2000).

[8] F. Platten, *et al.*, J. Chem. Phys. **142**, 174905 (2015).

[9] J. Hansen, *et al.*, J. Chem. Phys. **158**, 024904 (2023).

[10] S. Tanaka, M. Ataka, and K. Ito, Phys. Rev. E **65**, 051804 (2002).

[11] J. Hansen, S. U. Egelhaaf, and F. Platten, Phys. Chem. Chem. Phys. **25**, 3031 (2023).

[12] M. Muschol and F. Rosenberger, J. Chem. Phys. **103**, 10424 (1995).

[13] A. S. Parmar and M. Muschol, Biophys. J. **97**, P590 (2009).

[14] J. Hansen, F. Platten, D. Wagner, and S. U. Egelhaaf, Phys. Chem. Chem. Phys. **18**, 10270 (2016).

[15] O. Matsarskaia, *et al.*, Phys. Chem. Chem. Phys. **20**, 27214 (2018).

[16] J. Hansen, *et al.*, Phys. Chem. Chem. Phys. **23**, 22384 (2021).

[17] M. Madani, T. Hamacher, and F. Platten, Soft Matter **21**, 1937 (2025).

[18] T. Hamacher and F. Platten, Phys. Chem. Chem. Phys. **27**, 16558 (2025).

[19] A. Salis, *et al.*, Phys. Chem. Chem. Phys. **14**, 4343 (2012).

[20] F. Roosen-Runge, *et al.*, J. Phys. Chem. B **117**, 5777 (2013).

[21] F. Roosen-Runge, *et al.*, Sci. Rep. **4**, 7016 (2014).

[22] F. Sterpone, *et al.*, J. Mol. Biol. **311**, 409 (2001).

[23] M. Gerstein and C. Chothia, Proc. Natl. Acad. Sci. USA **93**, 10167 (1996).

[24] H. I. Okur, *et al.*, J. Phys. Chem. B **121**, 1997 (2017).

[25] K. D. Collins, Methods **34**, 300 (2004).

[26] M. M. Ries-Kautt and A. F. Ducruix, J. Biol. Chem. **264**, 745 (1989).

[27] M. Boström, D. R. M. Williams, and B. W. Ninham, Biophys. J. **85**, 686 (2003).

[28] Y. Zhang and P. S. Cremer, Proc. Natl. Acad. Sci. USA **106**, 15249 (2009).

[29] F. Evers, *et al.*, J. Phys. Chem. B **113**, 8462 (2009).

[30] A. Salis, *et al.*, J. Phys. Chem. B **111**, 1149 (2007).

[31] C. Duan and R. Wang, ACS Cent. Sci. **10**, 460 (2024).

[32] D. Ray, *et al.*, J. Phys. Chem. Lett. **15**, 8108 (2024).

[33] D. Ray, *et al.*, Soft Matter **21**, 3012 (2025).

[34] K. Kang and F. Platten, Sci. Rep. **12**, 3061 (2022).

[35] M. Taleb, *et al.*, J. Cryst. Growth **232**, 250 (2001).

[36] Z. Hammadi, *et al.*, Cryst. Growth Des. **7**, 1472 (2007).

[37] C. N. Nanev and A. Penkova, J. Cryst. Growth **232**, 285 (2001).

[38] C. N. Nanev, Crystals **7**, 310 (2017).

[39] F. Platten, *et al.*, J. Phys. Chem. B **119**, 14986 (2015).

[40] J. K. G. Dhont and K. Kang, Eur. Phys. J. E **33**, 51 (2010).

[41] K. Kang and J. K. G. Dhont, Soft Matter **6**, 273 (2010).

[42] A. Onuki, Eur. Phys. J. E **47**, 3 (2024).

[43] L. Hentschel, *et al.*, Phys. Chem. Chem. Phys. **23**, 2686 (2021).

[44] K. Kang, Rev. Sci. Instrum. **82**, 053903 (2011).

[45] B. Matthews, Acta. Crystallogr. **20**, 230 (1966).

[46] H. Fröhlich, *Theory of Dielectrics* (Oxford University Press, Oxford, 1958).